

# High-Order Structure and Dissociation of Gaseous Peptide Aggregates that are Hidden in Mass Spectra

Anne E. Counterman, Stephen J. Valentine, Catherine A. Srebalus, Sheila C. Henderson, Cherokee S. Hoaglund, and David E. Clemmer

Department of Chemistry, Indiana University, Bloomington, Indiana 47405, USA

Injected-ion mobility and high-pressure ion mobility techniques have been used to examine the conformations of bradykinin, insulin chain A, and several other peptide ions in the gas phase. Under the experimental conditions employed, evidence for multimer formation in the mass spectra of peptides is minimal or absent altogether. However, ion mobility distributions show that aggregates of peptides (containing a single charge per monomer unit) are observed at the same mass-to-charge ratios as the singly charged parent ions. Collision cross sections for these clusters show that they have tightly packed roughly spherical conformations. We have bracketed the average density as  $0.87 < \rho < 1.00 \text{ g cm}^{-3}$ . In some cases, specific stable aggregate forms within a cluster size can be distinguished indicating that some high order structures are favored in the gas phase. Multimer formation between different sizes of polyalanine peptides shows no evidence for size specificity in aggregate formation. Collisional and thermal excitation studies have been used to examine structural transitions and dissociation of the multimers. Aggregates appear to dissociate via loss of singly charged monomers. The observation that peptide multimers can be concealed in mass spectral data requires that fragmentation patterns and reactivity studies of singly charged monomers be undertaken with care. (*J Am Soc Mass Spectrom* 1998, 9, 743–759) © 1998 American Society for Mass Spectrometry

Observations of noncovalently bound complexes and multimers [1–21] formed by electrospray ionization [22] (ESI) have stimulated interest in the high-order structures of biomolecules in the gas phase [23]. In some cases there is evidence that highly specific noncovalent interactions that are present in solution are preserved in the gas phase [2–13, 15–17], while in other systems, nonspecific aggregates apparently form in the electrosprayed droplet [1, 14, 19]. Many exciting experiments appear to be accessible from studies of noncovalent associations of ESI ions, including solution enzyme/substrate, antibody/epitope, and receptor/ligand binding studies as well as the potential of stabilizing conformations or complexes in the gas phase that are atypical of those found in solution [11]. Studies of high-order biomolecular structures are limited because of the dearth of experimental options for probing these transient species in vacuo.

In this article we have used injected-ion mobility and high-resolution ion mobility techniques [24–27] to investigate the high-order structures and dissociation of multiply charged peptide aggregates, containing from two to six monomer units. Ion mobility measurements

allow information about the average shapes of biomolecules to be directly determined [24e, 25, 28, 29]. In the systems studied here, we find that the aggregates have compact, roughly spherical structures. In some cases, we find evidence for many stable aggregate conformations within a cluster size. This article presents the first direct look at the shapes of clusters of biomolecular ions.

Our initial intent in investigating peptide ions was to examine the relationship of peptide sequence to conformation in the absence of solvent. We briefly discuss monomer conformations below; however, this is not the focus of this article. As studies of several peptide systems progressed, it became clear that efforts were necessary to avoid multimer formation. In many cases our observations of aggregates in ion mobility data were surprising because the mass spectra exhibited little or no evidence for multimers. Below, we show that for some systems under the source conditions employed, most of the ion signal that is normally attributed to singly charged monomers is actually because of a series of related aggregates having a single charge per monomer unit.

Mass spectrometry (MS)-based strategies for rapidly deducing sequence information have become an important means of identifying unknown peptides and pro-

Address reprint requests to David E. Clemmer, Department of Chemistry, Indiana University, Bloomington, IN 47405.

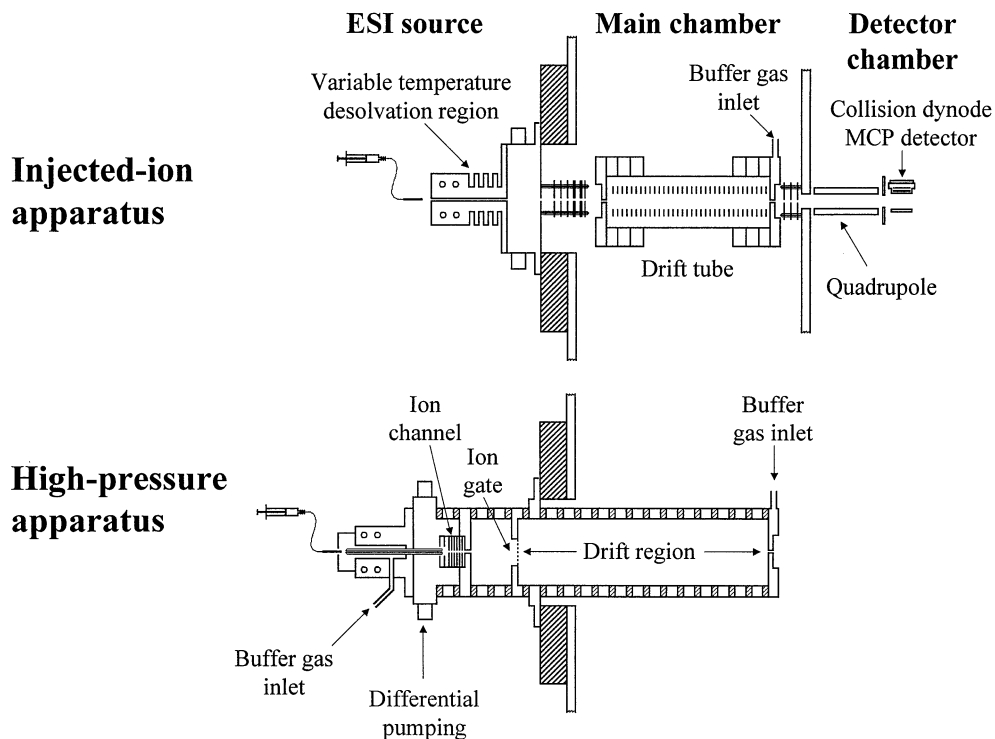


**Figure 1.** Schematic diagram of the injected-ion and high-pressure instrumental arrangements used for these studies. The mass filter and detector depicted in the top schematic are the same for both configurations.

teins [30]. A number of elegant studies have investigated the details of peptide and protein dissociation by using thermal, photon, and collisional activation methods [31]. The observation that peptide aggregates can be concealed in MS data should be of interest to these studies as the precursor state could influence energy deposition and fragmentation pathways.

In addition to ion mobility methods [24, 25, 28, 29], a number of MS-based methods have recently been used to investigate biomolecular conformations in vacuo. These include ion scattering experiments in triple quadrupole instruments [32]; kinetic energy release measurements [33]; microscopy studies of surfaces bombarded with high energy ions [34]; measurements of gas-phase H/D exchange levels [18, 35] and gas-phase basicities [36]; and studies of adduct formation [37, 38].

## Experimental

### General

Detailed discussions of ion mobility/MS methods [24] and their applications to biomolecules [25, 26, 28, 29] have been given previously. Only a brief description is given here. Two ion mobility configurations are utilized in these studies: an *injected-ion* configuration, in which ions are extracted into a high vacuum region and injected into the entrance of the drift tube at variable kinetic energies; and, a *high-pressure* configuration in which ions enter a drift region without being extracted

into a high-vacuum region. Schematic diagrams of both instruments are shown in Figure 1. In both configurations, ion mobility distributions are recorded by measuring the time required for a pulse of ions to travel across a well-defined drift region under the influence of a uniform electric field. Ions that exit the drift tube are focused into a mass spectrometer and detected by using an off-axis collision dynode detection system. Two vacuum chambers are used to house the instruments: a main chamber that houses and aligns all components of the ion mobility instrument and a detector chamber that contains the mass spectrometer, several focusing elements, and the detection system. For most of the studies reported here, ions of a known mass-to-charge are selected by a quadrupole mass filter. As discussed below, we have also used a time-of-flight instrument to perform measurements of mass-to-charge selected mobility distributions for mixtures of ions.

### *Injected-Ion Configuration*

The injected-ion instrument has been described previously [29]. Briefly, ions are formed by electrospraying solutions at atmospheric pressures into a variable temperature differentially pumped desolvation region (~2–10 torr). Ions exit this region through a 0.04-cm-diameter orifice into a high-vacuum region ( $10^{-5}$  to  $10^{-4}$  torr) where they are focused by a series of electrostatic lenses and accelerated to a desired kinetic energy.

Ion pulses (20 to 50  $\mu\text{s}$  in duration, obtained by varying the potential of a deflector in the lens system) are injected through a 0.020-cm-diameter aperture into the drift tube containing from  $\sim 1$  to 5 torr of He buffer gas. The ion charge state and voltage difference between the exit of the high-pressure source and the drift tube entrance flange define the injection energy. The drift tube used in these studies is 35.15 cm long and 30 equally spaced electrostatic lenses ensure a uniform electric field along the drift axis. In these experiments, drift fields ranging from  $\sim 3$  to 15  $\text{V cm}^{-1}$  were used. The maximum drift field is limited by the breakdown voltage of the He buffer gas, which is near the maximum fields used for these studies at these pressures.

As ions enter the drift tube, they are rapidly heated as their kinetic energies are thermalized by collisions with the buffer gas. Further collisions cool the ions to the temperature of the gas. This heating/cooling cycle can be varied by changing the injection voltage and is the basis for a straightforward approach for examining structural transitions [25, 28, 29, 39] and dissociation pathways of biomolecules [40]. In many systems it is desirable to inject ions at the lowest possible injection energy in order to examine conformations that are formed in the ion source. Attempts to characterize source conformations are limited by a minimum injection energy that is required to overcome the flow of buffer gas out of the drift tube entrance aperture; for most large molecules, ion signals decrease rapidly at injection voltages below  $\sim 50$  V.

### *High-Pressure Configuration*

Several recent studies have described high pressure drift tubes equipped with ESI sources [41]. In our instrument, the main vacuum chamber is designed in a modular fashion such that the high-pressure drift tube replaces the variable-temperature desolvation region, ion lenses, and drift tube of the injected ion instrument. Both configurations utilize the same buffer gas inlet systems and are aligned with the quadrupole using two V-block stands that are mounted to the chamber. It is possible to convert between the two instrumental configurations in a few hours.

The drift tube body is comprised of 2.5-cm-thick copper rings (12.7 and 15.2 cm inner and outer diameters, respectively) separated by 0.9-cm-thick ceramic spacers machined from mycalex (McMaster Carr, Chicago, IL). The copper/mycalex ring system is sealed by indium or silver wire, or viton O-rings, creating a sealed cavity that can be filled with buffer gas. The copper electrodes are designed to accept cartridge heaters, permitting temperature dependent studies. The drift region is 48.74 cm in length and is defined by the ion gate and exit of the drift tube. The drift field is created by voltages applied to the copper rings that are connected by a series of 5  $\text{M}\Omega$  high vacuum resistors (KDI/Triangle, Whippany, NJ, 1%). Calculations of the equipotential lines [42] created by using this geometry

show that the drift field is highly uniform along the drift axis, an important criterion for recording high-resolution ion mobility distributions [24d].

Ions are electrosprayed at atmospheric pressures directly into a differentially pumped desolvation region (analogous to the source described above) through a 17.8-cm-long, 0.16-cm-diameter capillary tube. The entrance of the tube protrudes into a plexiglass chamber that can be pressurized with He gas as shown in Figure 1. Ions are forced through the tube by the pressure gradient across the capillary.

The capillary extends into the center of a series of 10 BeCu lenses separated by 0.1-in.-thick Teflon spacers. The lenses and spacers create a 0.2-cm-diameter channel that is  $\sim 2.5$  cm long; most of the He buffer gas is pumped away through this region by the differentially pumped ion source. We estimate that the pressure in the differential pumping region is  $\sim 150$ – $200$  torr. The lenses are connected by a series of resistors in order to create a uniform electric field and the voltage drop across these lenses is  $\sim 1000$ – $2000$  V. This guides the ions from the source into the body of the drift tube against the counterflow of He buffer gas, while preventing neutrals from entering the drift region [27].

Once inside the body of the drift tube, the ions drift through the buffer gas under the influence of a field provided by the copper ring electrodes until reaching a wire gate. A variety of gating configurations can be used to cut a pulse of ions; the results reported here were obtained with a gate that is similar in design to one discussed previously by Hill and co-workers [24d]. The gate was constructed by stringing wire (nickel/iron alloy) to form sets of alternating, parallel rows spaced 0.07 cm apart on a fiberglass support. Opposite polarity voltage pulses are applied to the wires in order to introduce short pulses of ions into the drift tube. The pressure of the He buffer gas was  $\sim 200$  torr in these experiments.

### *Ion Mobility/Time-of-Flight Mass Spectrometry Measurements*

We have recently developed an ion mobility/time-of-flight (TOF) mass spectrometer that allows mass-resolved ion mobility distributions for large arrays of ions to be recorded simultaneously. A detailed description of this instrument has been given elsewhere [43]. Only a brief description is given here. Figure 2 shows a schematic diagram of this apparatus. Ions drift through the ion mobility instrument and are focused into the entrance region of a linear time-of-flight mass spectrometer. A series of lenses (G1–G4) are used to pulse and accelerate ions into a 43.2-cm-long field-free region for TOF analysis.

Because flight times in the mass spectrometer are much shorter than drift times in the ion mobility instrument, it is possible to record mass spectra within each drift time window. This allows mass resolved ion

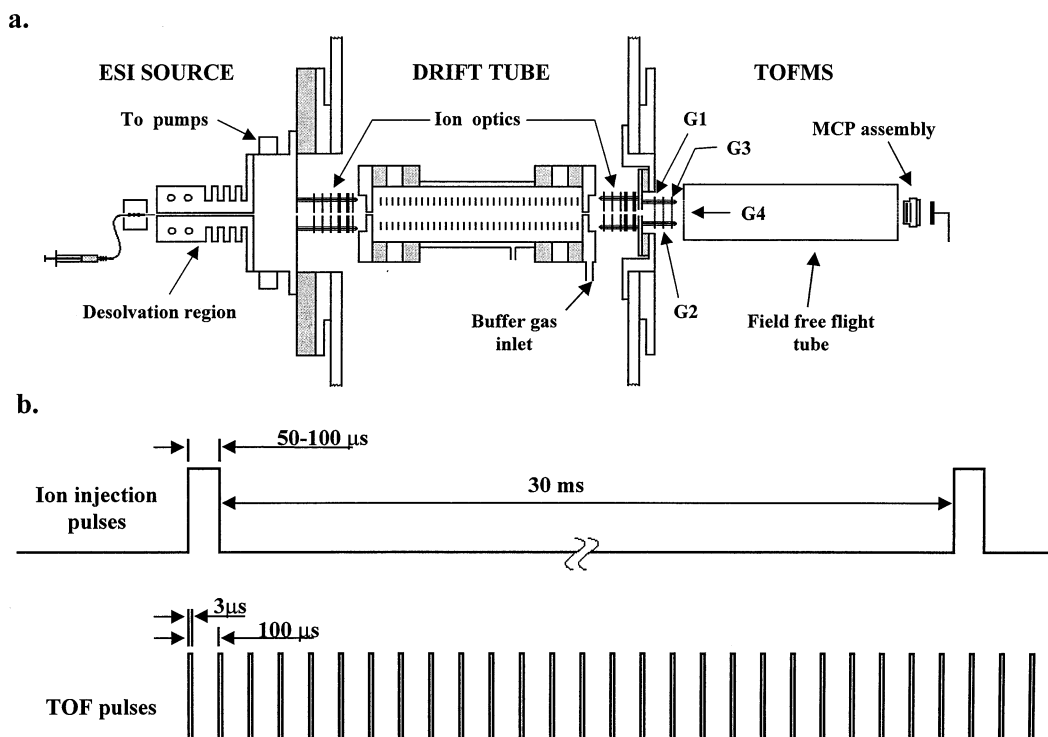


**Figure 2.** (a) Schematic diagram of the ion mobility/TOFMS instrument. (b) Pulse sequence used to record a three dimensional spectrum of drift times, flight times, and ion abundance for multiple mass-to-charge ions simultaneously.

mobility distributions to be recorded simultaneously for arrays of ions that are produced by ESI. In the present study we have utilized the injected ion drift tube and ESI source described above for the mobility measurements. An important advantage of this approach is that it facilitates direct measurements of mobility and mass resolved ion abundance for the system of ions.

Figure 2b shows a typical pulse sequence for initial injection of ions into the drift tube followed by time-of-flight analysis. Ions are injected into the drift tube at a repetition rate of 30 Hz and into the flight tube at  $10^4$  Hz. The initial injection pulse activates a programmable delay generator (PDG, Lecroy 4222) and pulse sequence that triggers a high voltage time-of-flight pulser at specified delay times. Flight times in the mass spectrometer are recorded by using a time-to-digital converter (TDC, Lecroy 4208) that is also initiated by the PDG pulse sequence. The instrumental electronics and data acquisition system are synchronized by an interface and controlled by a computer.

### Electrospray of Peptides

We have examined four peptides individually in this study: bradykinin (BK) (Sigma 98%, MW = 1060); and insulin chain A (ICA) [44] [Sigma >80%, molecular weight (MW) = 2532]; LG6 (TRQARRNAAAAWRE RQR, MW = 2052) and LG7 (TRQARRNRRRRAAAA AAA, MW = 1952), which were synthesized by using a

peptide synthesizer (Rainin, model PS3). Additionally, a range of polyaniline peptides were studied by electrospraying a mixture of peptides of varying sizes (Sigma, 1000-5000 MW). Positively charged (protonated) and negatively charged (deprotonated) peptide ions were formed by electrospraying solutions containing  $\sim 3 \times 10^{-5}$  to  $1 \times 10^{-3}$  M peptide in either 49:49:2 water:acetonitrile:acetic acid or 49:49:2 water:acetonitrile:ammonium hydroxide, respectively.

### Collision Cross Sections

In all of the configurations described above, the time required for ions to reach the detector is a composite of the drift time and time required for ions to travel through other portions of the instrument. Thus, it is necessary to account for the flight times of ions when no gas is present as well as for differences in the ions' energies at the exit of the drift tube in the presence and absence of buffer gas. These corrections are small ( $\sim 150$ - $250 \mu\text{s}$  for ions in the quadrupole-based instrument and  $\sim 80$ - $140 \mu\text{s}$  in the TOF instrument). Compact conformers have larger mobilities (and smaller collision cross sections) than more diffuse ones. The reduced mobility is determined from [25, 45]

$$K_0 = \frac{L}{t_{DE}} \frac{P}{760} \frac{273.2}{T} \quad (1)$$

where the measured parameters  $t_D$ ,  $E$ ,  $L$ ,  $P$ , and  $T$  correspond to the average drift time, the electric field strength, the drift tube length, buffer gas pressure (in torr), and temperature, respectively. Experimental collision cross sections are obtained directly from the ion mobility distributions from the relation [26]

$$\Omega = \frac{(18\pi)^{1/2}}{16} \frac{ze}{(k_b T)^{1/2}} \left[ \frac{1}{m_I} + \frac{1}{m_B} \right]^{1/2} \frac{t_D E}{L} \frac{760}{P} \frac{T}{273.2} \frac{1}{N} \quad (2)$$

which contains the mobility expression. The other terms are as follows:  $ze$ , the ion's charge;  $N$ , the neutral number density;  $k_b$ , Boltzmann's constant; and  $m_I$  and  $m_B$ , the masses of the ion and buffer gas, respectively. The parameters  $E$ ,  $L$ ,  $P$ , and  $t_D$  can be precisely measured such that the reproducibility of mobilities and cross sections is excellent. Any two measurements recorded on the same instrument typically agree to within 1% (percent relative uncertainty).

Cross sections measured with different instruments agree to within 2%. The present experiments were carried out at low  $E/N$  where mobilities are independent of the applied drift field and drift velocities are small compared with the thermal velocity of the buffer gas. Under these conditions, ions are not expected to align in the drift tube. Reduced mobilities for all peaks measured over a range of drift fields from 3–15 (injected-ion) and 20–200  $\text{V cm}^{-1}$  (high pressure) are identical within the experimental uncertainties. Thus, there is no evidence that ions align in the drift tube and we assume that cross sections correspond to an average of all possible orientations.

Structural information for different ions is obtained by comparing the experimental cross sections with cross sections that are calculated for atomic coordinates of trial conformations. Here, collision cross sections for trial structures are estimated by determining the orientationally averaged projection by using a method that is analogous to those described previously [24e, 25]. The reported values are an average of  $10^4$  to  $10^5$  random orientations. This method treats the interactions between atoms of the biomolecule and the buffer gas as hard-sphere collisions and assumes a rigid trial conformation. The values that are obtained depend slightly upon the hard-sphere diameters of the colliding partners and this approach is generally believed to provide a lower limit to the true collision integral. We have used diameters of 2.2 Å for He and H, and values of 3.1, 2.8, 2.7, and 3.1 Å for C, N, O, and S, respectively. Recently, methods for calculating cross sections for very large molecules have been scrutinized and attempts to include more realistic potential interactions and scattering trajectories in calculations of biomolecular cross sections have been made [46]. Shvartsburg and Jarrold have developed an exact hard sphere scattering model

(generally viewed as an upper limit) that rigorously accounts for momentum transfer associated with scattering of the buffer gas [47]. Cross sections from this method are ~12 to 15% higher (for elongated and compact conformations, respectively) than values obtained from the projection method.

### Theoretical Resolving Power

The ability to resolve two conformers having different collision cross sections is given by [48]

$$\frac{t_D}{\Delta t} \approx \left[ \frac{LEze}{16k_b T \ln 2} \right]^{1/2} \quad (3)$$

where  $\Delta t$  is the width of the drift time peak at half maximum. In the present experiments, we have used drift fields ranging from ~3 to 15  $\text{V cm}^{-1}$  in the injected-ion instrument and ~20 to 200  $\text{V cm}^{-1}$  in the high pressure instrument. The drift field is ultimately limited by the discharge potential of the buffer gas at a given operating pressure.

A measure of the theoretical resolving power can be obtained from calculated distributions for the transport of a single geometric structure through the drift tube. This is given by [45]

$$\Phi(t) = \int \frac{C}{(Dt)^{1/2}} (v_D + L/t) \left[ 1 - \exp\left(\frac{-r_0^2}{4Dt}\right) \right] \exp\left(\frac{-(L - v_D t)^2}{4Dt}\right) P(t_p) dt_p \quad (4)$$

where  $\Phi(t)$  is the intensity of ions passing through the exit aperture as a function of time,  $r_0$  is entrance aperture radius,  $v_D$  is the measured drift velocity,  $C$  is a constant,  $P(t_p)dt_p$  is the distribution function for the pulse of ions entering the drift tube, and  $D$  is the diffusion constant [49]. Comparisons of calculated distributions to experimental peaks provide information about the number of different conformations that are present. Experimental peaks that are significantly broader than the calculated distribution indicate either that multiple conformations exist or that conformers interconvert as they travel through the buffer gas. Close agreement between the calculated and experimental peaks suggests that only a single conformation is present. However, we cannot rule out the possibility that multiple conformations with identical mobilities are present.

## Results

### Similarity of Different Peptide Systems

The results discussed below focus on the BK and ICA systems. It is important to note that detailed studies of BK, ICA (as protonated and deprotonated ions), LG6 (as

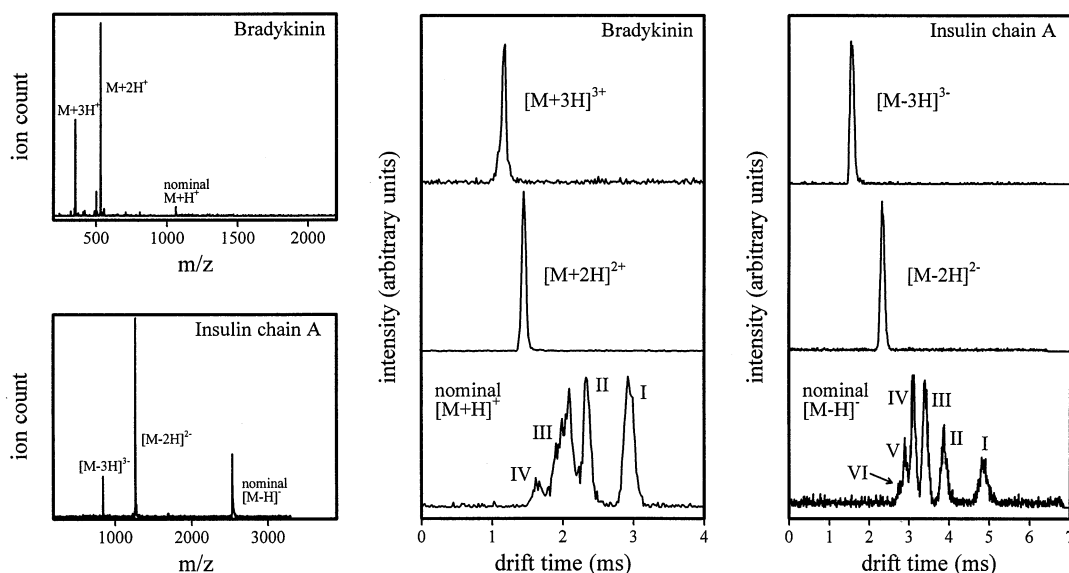


**Figure 3.** Plots on the left show ESI mass spectra for bradykinin and insulin chain A. The plot in the middle shows ion mobility distributions for the +3, +2, and nominal +1 BK ions. The plot on the right shows ion mobility distributions for the -3, -2, and nominal -1 charge states of insulin chain A. All ion mobility distributions have been normalized to a buffer gas pressure of 2.000 torr and a drift field of  $12.8 \text{ V cm}^{-1}$ . Data for bradykinin were recorded by using an injection voltage of 60 V. Data for insulin chain A were recorded by using an injection voltage of 160 V.

protonated ions), and LG7 (as deprotonated ions) show similar behavior to the results that are shown.

### Peptide Mass Spectra

Figure 3 shows example mass spectra for protonated BK and deprotonated ICA ions recorded by using the injected-ion mobility apparatus. Peaks for BK at  $m/z$  values of 354, 531, and 1061 are consistent with formation of triply, doubly, and singly protonated peptide ions, respectively [50]. A very small peak at  $m/z$  708 is consistent with formation of a triply protonated dimer ion  $[M_2+3H]^{3+}$ . Peaks in the mass spectrum for ICA at  $m/z = 843, 1265, \text{ and } 2531$  are consistent with formation of the deprotonated  $[M-3H]^{3-}$ ,  $[M-2H]^{2-}$ , and  $[M-H]^{-}$  ions, respectively. In several other ICA mass spectra (not shown) we have observed peaks in the mass spectra that can be assigned to  $[M_n - (n-1)H]^{(n-1)-}$  ( $n = 4-8$ ) and  $[M_n - (n+1)H]^{(n+1)-}$  ( $n = 2-4$ ) ions. These peaks are extremely small (usually less than 1% of the maximum peak height) such that evidence in the mass spectra for multimer formation is minimal (and often absent altogether).

### Injected-Ion Mobility Distributions

Ion mobility distributions for the major peaks observed in the mass spectra for BK and ICA are also shown in Figure 3. In all of the systems studied here, ion mobility distributions for doubly and triply charged monomer ions show a single peak. Drift times decrease with increasing charge state, a result of the larger effective

field strength ( $zE$ ) experienced by higher charge state ions. Multiple peaks are observed for  $m/z = 1061$  and 2531 ions of BK and ICA, respectively. The observation of multiple peaks for these mass-to-charge ratios is somewhat surprising, and requires that species with very different mobilities are present.

We have numbered the peaks for the  $m/z = 1061$  and 2531 ions from low to high mobilities (I-VI) as shown in Figure 3. Bowers and co-workers have previously reported a cross section of  $242 \text{ \AA}^2$  for singly protonated BK formed by matrix assisted laser desorption ionization (MALDI) [25]. From molecular modeling studies, they concluded that this ion has a compact conformation where the peptide has folded around the protonation site. By using a rearranged form of eq 2 and the  $242 \text{ \AA}^2$  cross section, we calculate an expected drift time for a singly charged compact conformation of 2.97 ms, in agreement with the peak observed at longest times.

To obtain additional information about these ions, we have varied the voltage that is used to inject ions into the drift tube. Figure 4 shows ion mobility distributions for the  $m/z = 1061, 2531, \text{ and } 1951$  ions of BK, ICA, and the LG7 peptide as a function of injection voltage. These data are typical of results we have obtained for all of the systems reported here. At injection voltages below the lowest values shown (60, 160, and 70 V for the BK, ICA, and LG7 systems, respectively) the distribution of peaks does not change significantly. Thus, we expect these distributions are near the distributions of ions formed in the source. Peaks I, II, and III are favored for BK; II, III, and IV are favored for

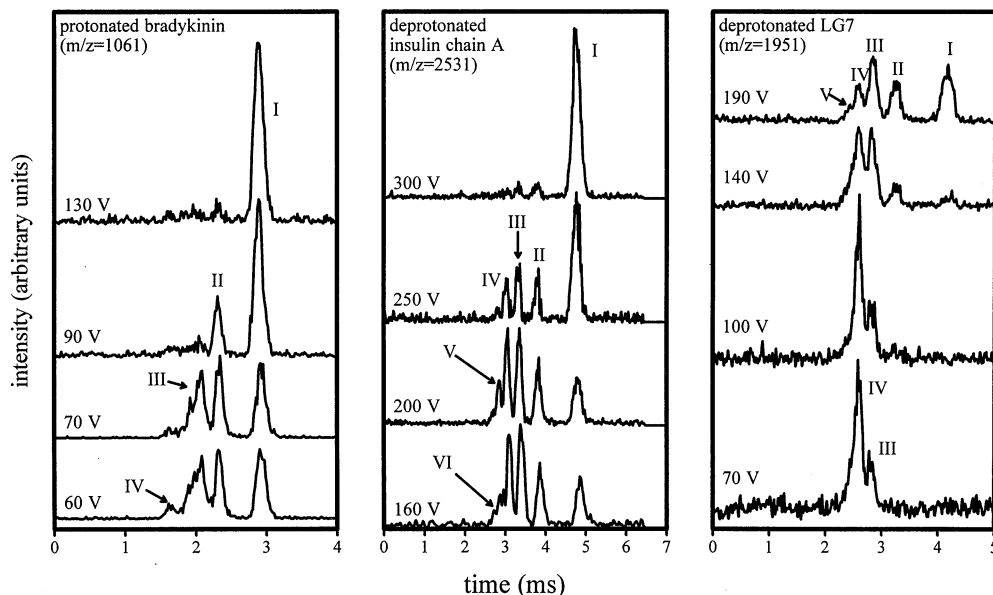


**Figure 4.** Ion mobility distributions recorded as a function of injection voltage for  $m/z = 1061$  ions of bradykinin (left),  $m/z = 2531$  ions of insulin chain A (middle), and  $m/z = 1951$  ions of LG7 (right). All spectra were normalized to a buffer gas pressure of 2.000 torr and a drift field of  $12.8 \text{ V cm}^{-1}$ .

ICA; and peak IV is favored for LG7. When the injection voltage is increased, the fraction of ions in peaks II–IV (BK), II–VI (ICA), and III and IV (LG7) decreases. At high injection voltages, peak I is favored for all systems. Mass spectra recorded at these injection voltages show no additional peaks associated with fragmentation that can account for the large changes observed in Figure 4 [51]. The differences between low and high injection voltage distributions must involve conversion of peaks II–VI into peak I.

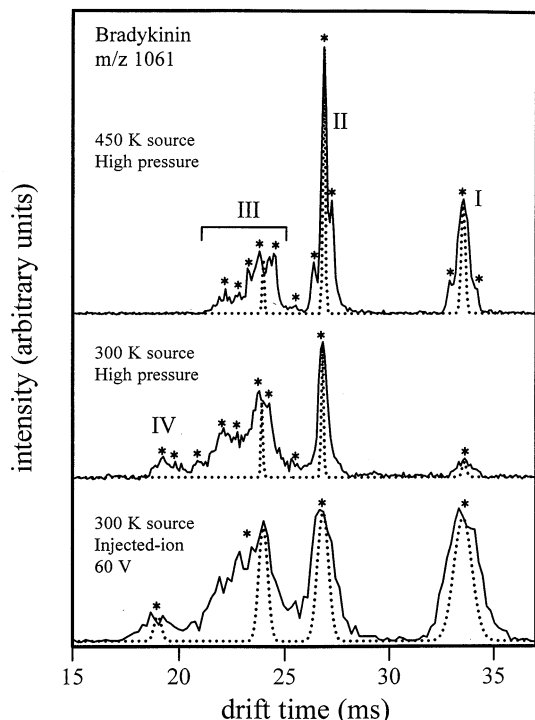
#### High Resolution Ion Mobility Distributions

Figure 5 shows high-resolution ion mobility distributions recorded at high pressures for  $m/z = 1061$  ions of BK. The data shown were recorded by using capillary temperatures of 300 and 450 K. Also shown are data recorded in the injected-ion instrument that are scaled for differences in length, pressure, and electric field strength for comparison. Overall, the peak shapes and positions recorded in the high-pressure instrument are in close agreement with the injected ion data. The primary difference between these data is the fraction of peak I ions: 32% of the distribution for the injected ion instrument, compared with only 7% for the high-pressure instrument. This difference presumably arises because of a small degree of multimer dissociation that occurs in the injected-ion instrument (even at the low 60 V injection voltage) that converts a small fraction of peaks II–IV into peak I. This does not occur in the high pressure instrument because ions are not exposed to the injection process.

A second difference in these data is the number of resolvable features. In the injected ion data, there are

four resolved features (peaks I–IV). All four of these peaks are noticeably broader than the calculated distributions obtained from eq 4 for transport of a single conformation. This indicates that multiple conformations are present, but not resolved, or that structures interconvert as they travel through the drift tube. The region associated with peak III (from  $\sim 21$  to 25 ms) is especially broad and has a full width at half maximum (FWHM) that is  $\sim 5$  times larger than the peak calculated for a single conformer. Many additional features can be discerned in the high resolution data. Under similar source conditions to the injected ion experiments (i.e., a capillary temperature of 300 K and identical solution composition), there are ten reproducible local maxima in the high pressure distribution. The region associated with peak III (from  $\sim 21$  to 25 ms) is  $\sim 40$  times larger than the  $\sim 0.1$  ms FWHM calculated for transport of a single conformer [52]. There are at least four reproducible maxima within peak III and at least three reproducible local maxima for peak IV.

Figure 5 also shows an ion mobility distribution that was recorded at a capillary temperature of 450 K. Under these conditions, peak IV is no longer observed, and the relative abundance of peak III is substantially less ( $\sim 20\%$  at 450 K compared with 35% observed at 300 K). The absence of peak IV, decrease in peak III, and an increased abundance of peaks I and II are all consistent with a thermal process in the ion source that is analogous to the changes induced by collisional activation (Figure 4). Within peaks I, II, and III, there are twelve reproducible features at 450 K. At least six reproducible features are observed for peak III and three distinct peaks for peak II. It is interesting that at high temperature, peak II shows three distinct peaks over a 26.1 to



**Figure 5.** Comparison of ion mobility distributions recorded by using the injected ion instrument and the high-pressure drift tube for  $m/z = 1061$  ions of bradykinin. The bottom spectrum shows data recorded in the injected ion instrument ( $IV = 60$  V). These data have been normalized to the high pressure conditions by accounting for differences in pressure, length, and voltage of the injected-ion and high-pressure drift tubes. The middle spectrum shows the ion mobility distribution obtained in the high-pressure instrument when the capillary temperature is 300 K. The top spectrum shows the distribution obtained at a capillary temperature of 450 K. All three data sets were normalized to a buffer gas pressure of 180.00 torr and a drift field of  $142.4 \text{ V cm}^{-1}$ . The dotted lines represent distributions calculated from eq. 4 for transport of a single conformation of each species through the drift tube (see text). Asterisks denote the locations of reproducible maxima in the distributions.

27.7 ms time range, whereas at room temperature, this feature was a single narrow peak. It is possible that these new features are produced from loss of peak IV. It is also possible that peak II anneals into three favored forms at higher capillary temperatures.

#### *Ion Mobility/Time-of-Flight Measurements for a Mixture of Polyalanine Sizes*

By using the ion mobility/TOF mass spectrometer shown in Figure 2 we have examined a mixture of polyalanine peptides (having different lengths) in order to rapidly assess whether the features observed for individual peptides are general for a wide range of peptide sizes. Figure 6a,b shows three-dimensional plots of a drift time/time-of-flight spectrum (at two orientations) for all ions that are observed after injecting the electrosprayed polyalanine ions into the drift tube with a voltage of 70 V. In this plot the ions' flight times

(in the TOF mass spectrometer) increase from right to left. From this orientation, we observe a series of resolved peaks that have flight times and drift times that increase systematically. From the flight times, we deduce a spacing of  $71 m/z$  (the molecular weight of a single alanine residue) between the resolved peaks [Figure 6(a)]. Thus, this series of peaks corresponds to singly charged alanine peptides of varying sizes  $[\text{Ala}_n + \text{H}]^+$ , and from these flight times, we deduce that  $n$  ranges from 5–30. The relative abundance of different peptide monomers has a bell-shaped distribution that peaks near the  $[\text{Ala}_{12} + \text{H}]^+$  peptide ion.

The  $[\text{Ala}_5 + \text{H}]^+$  to  $[\text{Ala}_{30} + \text{H}]^+$  size distribution is skewed toward much smaller peptides than we expected for ESI of a mixture of peptides in the 1000 to 5000 MW range ( $\text{Ala}_{13}$ – $\text{Ala}_{65}$ ) of the sample. It is likely that the smaller alanine peptides are favored by ESI because of differences in solubility. It is also possible that large peptide ions fragment into smaller ones on injection; however, this is unlikely because these injection conditions are far below where we typically observe significant covalent bond fragmentation.

The orientation of the plot in Figure 6(b) shows an additional distribution of ions. These ions have a TOF profile that is similar to the distribution of singly charged peptides; however, the drift times for these ions are shifted to shorter times. A magnification of these data [Figure 6(c)] shows individual mass spectra recorded within individual drift time windows. This plot shows that every other peak of the series of high mobility ions is observed at the same mass-to-charge units as the singly charged polyalanine peptides. Between peaks for the singly charged polyalanine peptides, we observe an additional series of peaks that have intermediate mass-to-charge spacings of  $\sim 36$  and indicate that this series of ions is due to a distribution of doubly charged ions. Because polyalanine peptides contain only a single basic site (the N-terminal amino group), the doubly charged ions observed must correspond to peptide aggregates having general formulas of  $[\text{Ala}_{2n} + 2\text{H}]^{2+}$  (observed at the same mass-to-charge ratios as the  $[\text{Ala}_n + \text{H}]^+$  ions) and  $[\text{Ala}_{2n+1} + 2\text{H}]^{2+}$  (observed at mass-to-charge ratios between the  $[\text{Ala}_n + \text{H}]^+$  peaks). Here,  $n$  ranges from  $\sim 9$  to 22 for the doubly charged dimer ions. The ability to resolve the  $[\text{Ala}_{2n+1} + 2\text{H}]^{2+}$  in the mass spectrum and the clear correlation in drift times of these ions with the higher mobility peaks that we assign to  $[\text{Ala}_{2n} + 2\text{H}]^{2+}$  ions further corroborates the assignment of higher mobility ions to multiply charged multimers in these systems.

In some cases, we observe a third feature in the data that shows up as a low intensity unresolved feature that is broadly distributed over a wide range of drift and flight times. The present data show that this broad feature is centered near a flight time of  $\sim 15 \mu\text{s}$  ( $m/z \sim 1200$ ) and a drift time of  $\sim 3$  ms. These ions are not easily assigned because the peak is poorly resolved. The peak may correspond to a system of larger aggregates or to partially solvated ions.

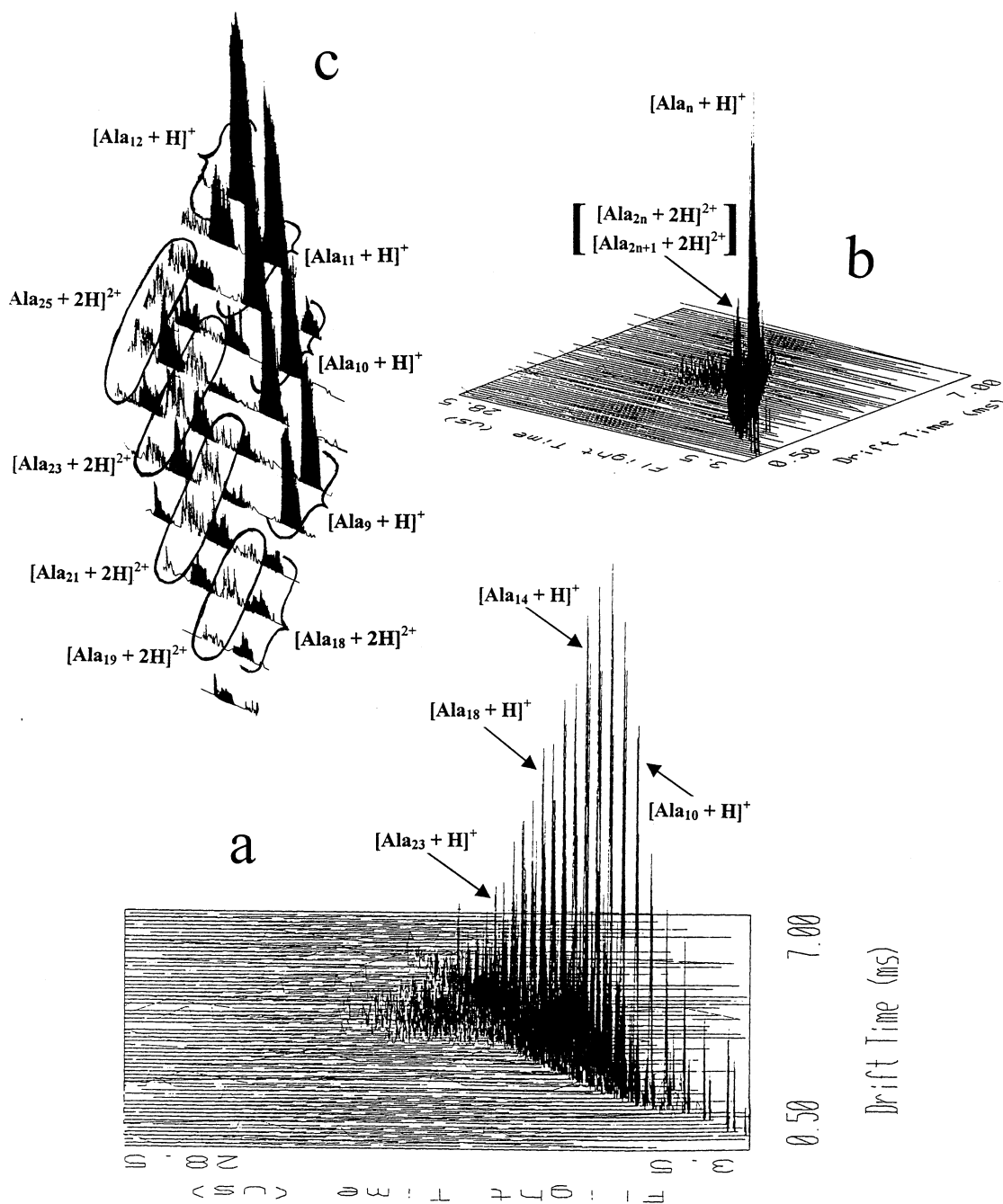


**Figure 6.** (a) Three-dimensional plot of drift time, flight time, and ion abundance for a distribution of electro sprayed polyaniline ions measured by using the ion mobility/time-of-flight MS instrument shown in Figure 2. The drift tube was operated by using a drift field of  $11.8 \text{ V cm}^{-1}$ , and  $1.900 \pm 0.004$  torr of He buffer gas. The data were recorded at an injection voltage of 70 V. The resolved peaks correspond to  $[Ala_n + H]^+$  peptides having  $n = 5-30$ . (b) shows the same distribution at a slightly different orientation. Here, the peaks observed in (a) comprise the single large peak on the right. This orientation allows a second distribution of ions corresponding to  $[Ala_{2n} + 2H]^{2+}$  and  $[Ala_{2n+1} + 2H]^{2+}$  dimer ions to be resolved. Fig. 6(c) shows a blow up of the three dimensional plot over the  $[Ala_9 + H]^+$  to  $[Ala_{12} + H]^+$  size range. These data show TOF spectra associated with eleven distinct drift time windows. Shaded peaks represent features at the same mass-to-charge ratios associated with  $[Ala_n + H]^+$  monomers and  $[Ala_{2n} + 2H]^{2+}$  dimer ions. The brackets show the range of drift times associated with these ions. The white peaks observed at mass-to-charge ratios between those for the  $[Ala_n + H]^+$  ions are because of  $[Ala_{2n+1} + 2H]^{2+}$  ions. The range of drift times associated with these peaks is circled.

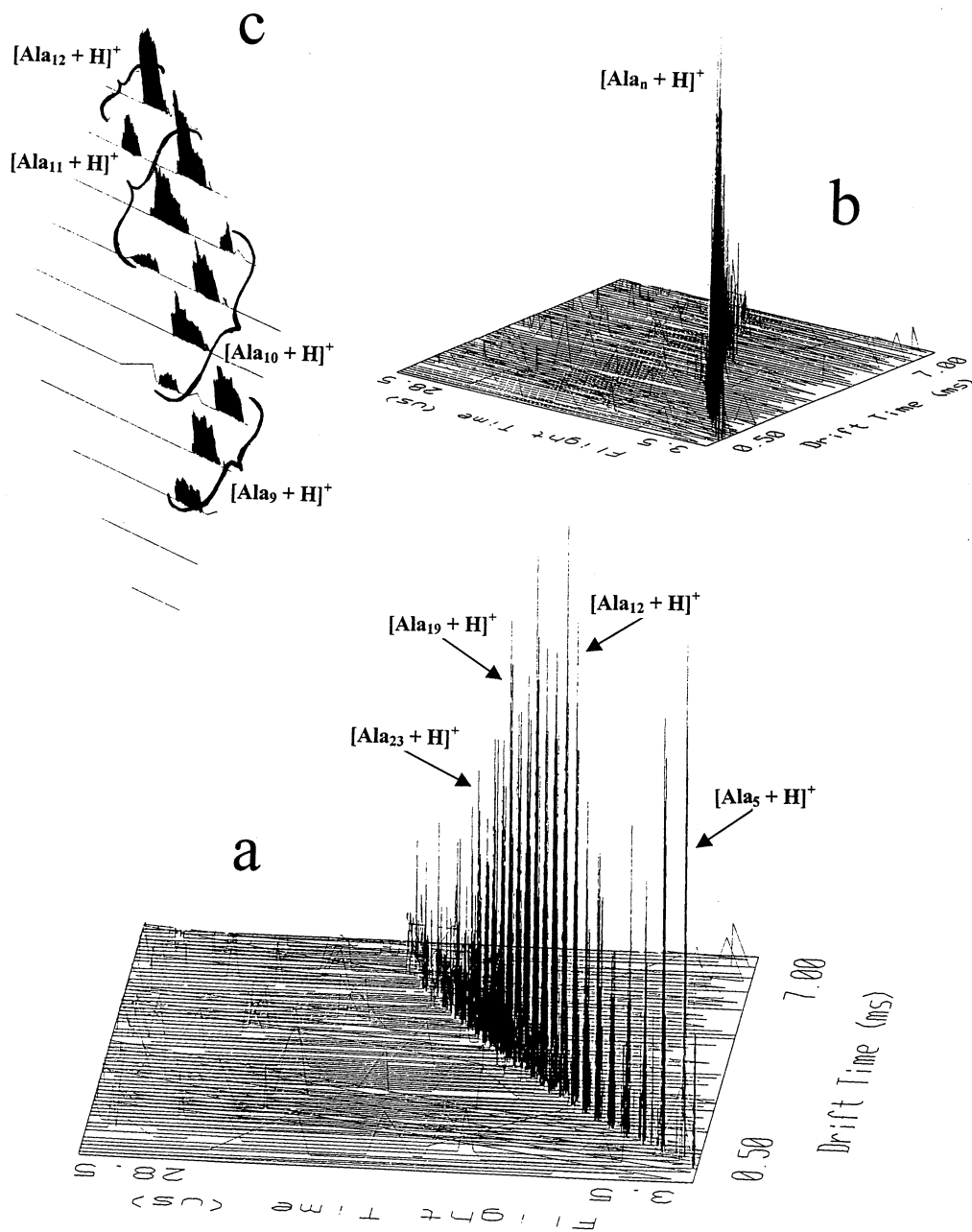


**Figure 7.** Three-dimensional representation of drift time, flight time, and ion abundance for a distribution of electro sprayed polyaniline ions injected into the drift tube by using 280 V. The data were recorded by using a drift field of  $11.8 \text{ V cm}^{-1}$  and a buffer gas pressure of  $1.973 \pm 0.005$  torr. (a), (b), and (c) are the three orientations shown in Fig. 6.

Figure 7a,b,c shows the ion mobility/TOF distribution that is obtained when the mixture of ions is injected into the drift tube at 280 V. At this injection voltage, features in the data corresponding to the higher mobility doubly charged dimer ions are depleted and the peaks assigned as singly charged polyaniline containing 5 to 30 residues remain. The size range of singly charged alanine peptides ( $[\text{Ala}_5+\text{H}]^+$  to  $[\text{Ala}_{30}+\text{H}]^+$ )

and distribution maximum (at  $[\text{Ala}_{12}+\text{H}]^+$ ) are the same as observed at an injection voltage of 70 V. This indicates that peptide fragmentation across covalent bonds is minimal. A final interesting feature of these data is that smaller peptides appear to be favored at high injection voltages. Presumably, these ions are formed upon dissociation of larger doubly charged aggregates.

## Discussion

### *Cross Sections for Monomer Ions*

By using eq 2 and the data in Figure 3, we derive cross sections of 239, 240, and 284 Å<sup>2</sup> for the BK(+1), BK(+2), and BK(+3) ions. The 239 and 240 Å<sup>2</sup> values determined for BK(+1) and BK(+2) are similar to the 242 Å<sup>2</sup> value for BK(+1) reported by Bowers and co-workers [25]. The BK(+1) ion is believed to be stabilized by formation of a gas-phase salt bridge where the C-terminal carboxylic acid group is deprotonated and stabilized by interactions with protonated Arg1 and Arg9 residues [53]. The BK(+2) ion does not appear to form a salt bridge and an extended conformation, which reduces Coulomb repulsion energy has been proposed [53]. Although we have not carried out detailed molecular modeling studies for this system, the 240 Å<sup>2</sup> cross section for BK(+2) indicates that this state is as compact as the BK(+1) ion. This ion may relieve some repulsive forces by placing charges on opposite sides of the compact form. The BK(+3) ion has a cross section of 284 Å<sup>2</sup>, ~20% larger than the cross sections observed for the compact BK(+1) and BK(+2) states. This ion cannot form a salt bridge because all three basic sites (Arg1, Arg9, and the N-terminal amino group) are protonated during the ESI process, leaving the C-terminal carboxylic acid group protonated. Without the salt bridge, the peptide adopts more elongated conformations in order to reduce the Coulomb repulsion energy.

Bowers and co-workers resolved a single peak for BK(+1) and noted that it was broader than the distribution calculated for a single conformation [25]. Our high-resolution ion mobility distribution shows shoulders on both sides of the main features for the main peak for BK(+1), a result that requires that at least three conformations are stable over the 20–30 ms time scale of these experiments. The BK system has three basic sites (Arg1, Arg9, and the N-terminal amino group) and a single acidic site (the C-terminal carboxylic acid) that give three different possible salt-bridge combinations. All would involve interactions between both ends of the peptide and thus lead to compact conformations. It is possible that other compact structures that do not involve a salt-bridge account for one or more of the shoulders observed. In their thermal dissociation studies, Williams and co-workers have noted an induction period prior to the onset of dissociation that they postulated might be due to the time required for other conformations to reach the dissociative state [53]. The observation of three stable states in our data may help explain the origin of the delay observed by Williams.

By using molecular modeling methods we have generated several closely packed folded conformations, conformers that are primarily  $\alpha$ -helical, and near-linear structures for each of the four peptides studied here. These modeling methods were not as extensive as those employed by Bowers for BK [25] or the approach used in our DNA studies [54]. However, they provide a good

estimate of cross sections for compact and elongated conformations and allow us to rapidly assess the nature of conformations studied here. Overall, the best agreement with the experimental data is found for trial conformers that have compact (roughly spherical) conformations, such as those discussed above for BK(+1) and BK(+2). Cross sections of 388 and 390 Å<sup>2</sup> measured for the ICA(–2) and ICA(–3) ions also appear to be tightly packed (roughly spherical) forms. Trial elongated  $\alpha$ -helical and near-linear conformers have cross sections that are factors of  $1.2 \pm 0.1$  and  $1.5 \pm 0.1$  times larger than those estimated for compact conformations of the peptides studied here. If the exact hard sphere scattering model (which gives higher values) is used to calculate cross sections, then conformations must be even more tightly packed in order to match the experimental cross sections.

Several of the highly charged peptide monomers do not favor compact conformations. These include BK(+3) (discussed above) and ICA(–4), that was formed under some ESI conditions and has a cross section of 470 Å<sup>2</sup>. These ions favored conformations that are highly extended (between values we estimate for trial helical and near-linear forms).

### *Assignment of Peaks II–IV for BK (m/z = 1061) and I–VI for ICA (m/z = 2531)*

Assuming peak I for ICA(–1) corresponds to a singly charged monomer, we derive a cross section of 390 Å<sup>2</sup>. This value is the same as the 388 and 390 Å<sup>2</sup> cross sections derived for ICA(–2) and ICA(–3). Thus, from the above discussion, ICA(–1) must be a compact conformation of the monomer peptide.

Attempts to create more compact forms of singly charged monomer ions to assign to higher mobility ions have been unsuccessful. This indicates that peaks II–VI are due to more highly charged ions. In order to have mass-to-charge ratios that are identical to the singly charged monomers, these ions must have the general formula  $[M_n + nH]^{n+}$ . Mobilities for multiply charged multimers are determined by each multimer's charge-to-cross section ratio. In systems where the average cross section per monomer unit decreases as the monomers associate, the mobilities will sequentially increase as the cluster size increases (as observed in Figures 3 and 4). Mobilities for peaks II, III, and IV are larger than values for peak I by factors of  $1.3 \pm 0.1$ ,  $1.5 \pm 0.1$ , and  $1.7 \pm 0.1$  for the systems studied here. Multiply charged aggregates (containing a single charge per monomer) are also expected to dissociate to form singly charged peptides, with no obvious changes in mass spectral distributions, consistent with the injection voltage studies (Figure 4). With the peaks assigned as multiply charged multimers, we note that dissociation appears to occur by sequential monomer loss, as there are no favored multimer peaks at intermediate injection voltages.

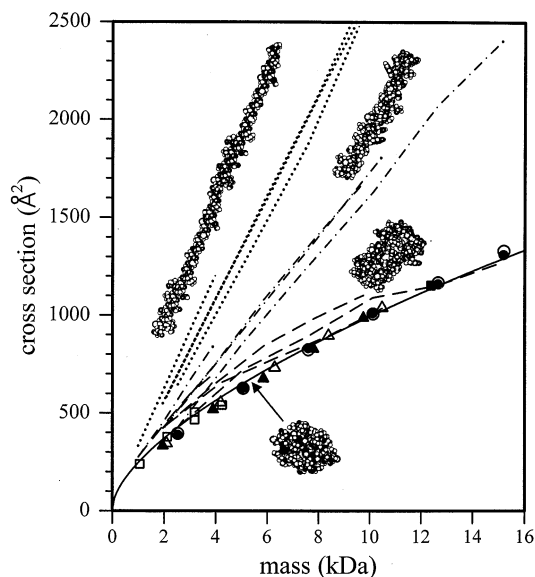


**Figure 8.** Cross sections as a function of mass for monomers and multimers of bradykinin (open squares), insulin chain A [protonated (open circles) and deprotonated (filled circles)], LG6 (open triangles), and LG7 (filled triangles). The cross section of the +4 state of cytochrome *c* is also shown (filled square). The solid line represents cross sections calculated for spherical ions having a density of  $0.87 \text{ g cm}^{-3}$ . Dashed, dotted-dashed, and dotted lines show calculated cross sections assuming aggregate structures are bundles of helices attached side-to-side, helices attached end-to-end in series, and a series of extended strings for each of the peptide systems. See text for discussion.

To proceed further in the analysis of these systems, we assumed that the cluster size corresponds to the peak numbers. In most of the systems we have studied, peaks are easily resolved and assigned by this approach. However, some ambiguities associated with unresolved features, such as peaks III and IV (BK); V and VI (ICA); and IV and V (LG7) exist. In all cases, assignments have been made from multiple data sets. In some of the ICA data, peaks V and VI were resolved to baseline, clarifying this system. The assignments of peaks III and IV for BK are considered in detail below. The assignment of peak IV and peak V for LG7 (the peak and shoulder shown in Figure 4) is ultimately based on the similarities with the other peptides studied.

Figure 8 shows aggregate cross sections determined from Eq 2 plotted against mass. Cross sections increase systematically with increasing mass, suggesting that the overall shapes of these aggregates are the same for all of the peptides studied. Insight into the shapes of the aggregates can be obtained by comparing the experimental cross sections with several models. Figure 8 also shows calculated collision cross sections for a variety of trial aggregate structures, including systems of near-linear and helical monomers attached end-to-end, bundles of helical monomers in a closest packed arrangement, and spherical monomers in a closest packed arrangement. This analysis shows that elongated end-

to-end arrangements are much larger than any of the ions observed experimentally. As discussed below, these structures should reduce Coulomb repulsion of the multiply charged systems, but allow for only a few noncovalent binding interactions between monomers. An excellent fit to the experimental data is obtained by considering the cross section of a sphere of constant density as a function of mass. By using the expression  $\Omega = \pi[(3m/4\pi\rho)^{1/3} + 2.2/2]^2$  we derive an average aggregate density of  $\rho = 0.87 \text{ g cm}^{-3}$ . This method of analysis is essentially the projection model described above, and thus the density obtained should be a good lower limit to the true aggregate density. Cross sections for trial aggregates, where spherical monomers are arranged into tightly packed roughly spherical arrangements, are also in good agreement with the experimental results. An upper limit to the average density can be obtained by considering that the exact hard sphere scattering model (applied to roughly spherical compact conformers) typically yields cross sections that are  $\sim 15\%$  larger than values obtained from the projection approximation method. This brackets an upper limit for the density as  $1.00 \text{ g cm}^{-3}$ . The  $0.87 < \rho < 1.00 \text{ g cm}^{-3}$  density found here is somewhat below densities that have been reported for biomolecules in solution [55].

A final note regarding this analysis involves cross sections calculated for bundles of elongated conformations. Unlike cross sections for aggregates of elongated conformers bound end-to-end (that diverge rapidly from the experimental data with increasing size, Figure 8), bundles of elongated monomers bound side-to-side are in poor agreement with the experimental data for small multimers, but are in reasonable agreement for large multimers. As the number of elongated monomers in the bundle increases, the aggregate takes on a compact three-dimensional structure. Side-to-side interactions of elongated monomers provide numerous opportunities for noncovalent van der Waals and hydrogen bonding interactions that may stabilize the multiply charged system. For example,  $\beta$ -sheet-like interactions (that maximize hydrogen bonding between two aligned peptides) may be favored for these types of structures.

### *Complications in Assignments of Aggregate Cluster Size*

Difficulties in peak assignments in these systems are compounded by the possibility that highly charged multimers could adopt elongated conformations in order to reduce Coulomb repulsion. This type of behavior has been observed for a number of multiply charged protein systems [28, 29] and DNA [54]. We have considered this in some detail in order to avoid misassigning peaks in these systems. A particularly difficult system is BK. In Figure 5, peaks I and II contain multiple stable conformations that have cross sections that are near the values calculated for tightly packed spherical forms. Thus, there is little ambiguity in assign-

ing features in peaks I and II as  $[M+nH]^+$  monomers and  $[M_2+2H]^{2+}$  dimers, respectively. However, none of the features observed from  $\sim 18$  to 25 ms in Figure 6 associated with peaks III and IV are resolved at baseline, making the near continuum of peaks more difficult to assign.

It is possible that all of the features observed over the  $\sim 18$  to 26 ms range associated with peaks III and IV in the BK system (Figure 5) are due to a range of different conformations within a single multimer size (i.e.,  $[M_4+4H]^{4+}$ ). The absence of  $[M_3+3H]^{3+}$  would be consistent with a formation process in which monomers aggregate to form dimers, and dimers aggregate to form tetramers. In the present system, drift times of 22.8 and 23.7 ms (for the features observed in peak III at high resolutions) would have cross sections of  $\sim 650$  and  $700 \text{ \AA}^2$ , similar to values calculated for extended helical forms of the tetramer (Figure 8). Extended forms of BK aggregates may be especially stable if ionic interactions such as salt-bridge structures between monomer units stabilize the aggregates. In the end, based on the correlation with other systems in Figure 8 and the dissociation data in Figures 3 and 4 we believe the best assignment of the broad feature observed for peak III is to the trimer ion  $[M_3+3H]^{3+}$ .

### *Heterogeneous Aggregates of Different Peptide Sizes of Polyalanine*

The three-dimensional drift time and time-of-flight data recorded for the mixture of different sizes of polyalanine peptides provides insight about the size specificity of aggregate formation. The ability to record mass-to-charge resolved mobility distributions simultaneously in our ion mobility/TOF apparatus allows mobility and mass-to-charge resolved abundance information for all ions of the system to be directly measured. The cross sections derived from these data for all sizes of  $[Ala_n+H]^+$  peptides are consistent with values we have calculated for structures derived by detailed molecular modeling studies and will be discussed elsewhere [56]. Figure 6(c) shows peaks assigned as doubly charged dimer ions,  $[Ala_{2n}+2H]^{2+}$  and  $[Ala_{2n+1}+2H]^{2+}$ . There are no dramatic differences in abundance in these peaks, which would be expected if specific sizes preferentially formed aggregates. Further, the largest peak in these distributions is observed for the  $[Ala_{24}+2H]^{2+}$  ion, near the largest  $[Ala_{12}+H]^+$  peak observed for the monomer. Thus, it appears that aggregates of polyalanine peptides associate according to the initial populations of peptide monomers. We note that within a specific mass-to-charge ratio, the FWHM of the ion mobility peak for doubly charged polyalanine aggregates is larger than the FWHM observed for the singly charged polyalanine monomer ions. In all of the individual peptide ions that we have studied, FWHMs for peak II are less than FWHMs for peak I, because of the higher mobility and higher charge state of the multiply

charged multimer that leads to greater resolving power (eq. 3). The apparent broadening of the doubly charged dimer ions of polyalanine aggregates probably results from the heterogeneity of the monomer sizes within the different aggregate structures. For example, at  $m/z = 872$ , the  $[Ala_{24}+2H]^{2+}$  ion could be formed from aggregation of  $Ala_{10}+Ala_{14}$ ,  $Ala_{11}+Ala_{13}$ ,  $Ala_{12}+Ala_{12}$ , etc. Future high-resolution studies may clarify this.

### *Considerations of the Role of Solvents in Aggregate Formation*

Schey and co-workers have investigated multimer formation as a function of initial solution concentration and find that above a minimum threshold concentration the fraction of multimers is essentially invariant [14]. Below this threshold, multimers are not observed. We have monitored ion mobility distributions over a range of concentrations ( $3 \times 10^{-5}$  to  $1 \times 10^{-3}$  M) for BK and ICA. There are no significant variations in the multimer distribution. At concentrations below  $3 \times 10^{-5}$  M, the low abundance of  $m/z = 1061$  and  $2531$  ions (for BK and ICA, respectively) precludes measurements of ion mobility profiles.

Despite the lack of a concentration dependence, it is unlikely that multiply charged aggregates are formed by association of singly charged monomers in the gas phase because of the long-range nature of the repulsive Coulombic interactions [1, 23b]. Attractive van der Waals and hydrogen bonding interactions that stabilize the multimers will only become significant at short interaction distances. Thus, solvent shielding of charges should play an important role in formation of multiply charged multimers, either in bulk solution or as the ESI droplet dries [57].

### *Predicting the Stability of Multiply Charged Multimers*

The similarities between systems that we have observed suggests that a general model that predicts the stability of multiply charged peptides may be accessible by considering Coulomb repulsion as a function of multimer size. The solid lines in Figure 9 show Coulomb repulsion energies that we have calculated for two to eight charges placed on the surfaces of spheres of varying cross section [58]. As expected, for a sphere of a given size, the Coulomb energy increases with the number of charges. For spheres of a given charge, the Coulomb energy decreases as the size of the sphere increases. Superimposed on these lines are symbols that correspond to the experimentally measured cross sections for each of the  $[M_n+nH]^{n+}$  multimers observed for the different peptide systems. The average Coulomb repulsion energy per monomer unit increases with increasing multimer size for  $[M_n+nH]^{n+}$  ions. As the size of the individual monomer units become larger, the stabilities of  $[M_n+nH]^{n+}$  aggregates increase, and mul-

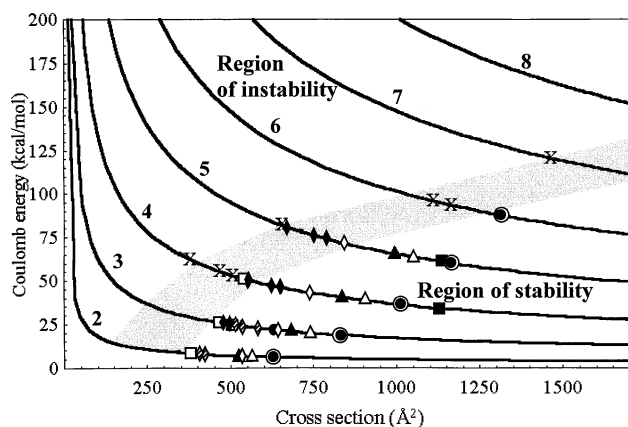


**Figure 9.** The solid lines show calculated Coulomb energies as a function of cross section for spheres containing two to eight charges. Cross sections are plotted on the respective charge line for experimentally observed multimers of protonated bradykinin (open squares), insulin chain A [protonated (open circles) and deprotonated (filled circles)], protonated LG6 (open triangles), and deprotonated LG7 (filled triangles). We have included the measured cross section for  $[M_2-3H]^{3-}$  for ICA, which was a small peak in the mass spectra for some experimental conditions. Also shown are cross sections estimated for  $[M_{(n+1)}+(n+1)H]^{(n+1)+}$  ions, where  $n$  corresponds to the number of monomer units comprising the largest  $[M_n+nH]^{n+}$  multimer observed experimentally for each peptide system. These points are shown as an "X" and correspond to ions that were not observed experimentally. The X's on the charge state 4 line represent the Coulomb energy for the  $[M_2+4H]^{4+}$  and  $[M_3+4H]^{4+}$  ions of bradykinin, that were also not observed experimentally. The open and solid diamonds show cross sections (estimated from Figure 8) for  $[M_n+(n-1)H]^{(n-1)+}$  and  $[M_n+(n+1)H]^{(n+1)+}$  ions (respectively) observed by Schey and co-workers [14]. The shaded diamonds correspond to cross sections for  $[M_5+2H]^{2+}$ ,  $[M_7+2H]^{2+}$ ,  $[M_7+3H]^{3+}$ , and  $[M_8+3H]^{3+}$  ions also estimated from Figure 8 for two peptides. The solid squares show cross sections for the +4 and +5 charge states of cytochrome *c*, taken from [28b]. A broad shaded region is used to illustrate a stability boundary that occurs at the interface of species that are observed experimentally and those that were not observed.

timers should persist to larger sizes. Indeed, the maximum aggregate sizes  $n = 4, 5,$  and  $6$  for the BK, LG7, and ICA, respectively, increase with the number of amino acids in each peptide (9, 17, and 21 for BK, LG7, and ICA, respectively). As the number of monomer units in the multimer increase, these ions become increasingly unstable, placing a limit upon the maximum possible  $[M_n+nH]^{n+}$  size for each peptide.

Additional insight into the stability of these ions can be seen by considering the cross sections and Coulomb repulsion energies that are expected when an additional  $[M+H]^+$  monomer is added to the largest  $[M_n+nH]^{n+}$  aggregate observed experimentally. These multimers were not observed experimentally and are assumed to be unstable. Estimates of cross sections for spherical forms of these ions can be obtained from Figure 8. Plots of these values along the Coulomb curves in Figure 9 show that addition of a singly charged monomer to the largest experimentally observed ion results in a multimer that falls to the left of experimentally observed

values for all sizes of each of the systems studied. This is expected if the binding interactions for a given area of contact between monomer units are similar for each of the peptides studied here. The resulting plot of species that are observed and those species that are constructed by addition of a monomer to the largest observed multimer defines a boundary associated with the transition between stable and unstable multimers. Spherical multimers with cross sections and charge states that fall to the right of this boundary are expected to be stable, whereas those on the left should be unstable. Highly charged spherical aggregates such as  $[M_n+(n+1)H]^{(n+1)+}$  ions should be less stable than  $[M_n+nH]^{n+}$  ions and should diminish more rapidly in intensity with increasing size than  $[M_n+nH]^{n+}$  multimers. Multimers containing fewer charges than monomer units (such as  $[M_n+(n-1)H]^{(n-1)+}$ ) should extend to larger sizes than the  $[M_n+nH]^{n+}$  ions observed here.

Intrinsic to the arguments presented above is the idea that the maximum multimer size is defined by each ion's stability in the gas phase. It is conceivable that multimer size distributions are limited by kinetic constraints during the ESI process such as initial peptide concentration. However, multimer size distributions for  $[M_n+nH]^{n+}$  appear to be independent of solution concentration, consistent with the idea that higher multimers are not observed because they are inherently unstable.

A feeling for the utility of Figure 9 as a predictor of peptide multimer stability can be obtained by considering multimer formation observed in MS studies by others. The closest comparison comes from mass spectra of several peptides measured by Schey [14]. Their data show mass spectra that are comprised of large fractions of  $[M_n+(n-1)H]^{(n-1)+}$  ( $n = 2-7$  for angiotensin I and  $n = 2$  and  $3$  for a NRKLLDIA-NH<sub>2</sub> sequence) as well as other multimers as large as octamers that contain only a few charges. As mentioned above, in some of our data we have observed small peaks corresponding to similar ICA ions. Assuming that these ions are spherical, the data in Figure 8 can be used to deduce collision cross sections that are also shown in Figure 9. For these ions, the multimer order is larger than the charge state and thus the ions have cross sections that fall to the right of the stability boundary. Several mass spectra show evidence for  $[M_n+(n+1)H]^{(n+1)+}$  ( $n = 2-5$  for renin substrate and  $n = 3$  and  $4$  for angiotensin I). The intensity variations in the mass spectra are similar to those we have observed for increasing multimer sizes of  $[M_n+nH]^{n+}$  aggregates in drift time distributions. Cross sections derived from Figure 8 for these ions fall near the stability boundary in Figure 9 because each multimer contains more charges than monomer units.

Figure 9 fails to predict the stability of several higher charge states of small multimers reported by Schey [14], including:  $[M_3+7H]^{7+}$  and  $[M_4+9H]^{9+}$  for renin substrate. If spherical, these ions would have cross sections of 652 and 790 Å<sup>2</sup>, and fall far above the stability

boundary on the 7 and 9 charge lines (Figure 9). It is worth noting that the mass spectral peak for  $[M_3+7H]^{7+}$  is exceedingly small (less than 2% of the largest peak shown) and we are unable to find the  $[M_4+9H]^{9+}$  in the data they show [14]. It could be argued that these ions are metastable and would not be observed on the longer time scales of our measurements, or that these ions have elongated structures and thus should not follow the model. Figure 9 also fails to predict large peaks observed for a number of highly charged dimers including the  $[M_2-7H]^{7-}$  ion of ICA and very highly charged protein dimers such as the +20 to +24 states of cytochrome *c* [7]. It is likely that these highly charged ions do not have spherical conformations. Based on the extended state reported above for ICA(-4), we expect extended conformers of the dimer -7 charge state. We have measured cross sections for highly charged dimers of cytochrome *c*. Comparison of experimental cross sections for  $[Cyt_2+19H]^{19+}$  with trial dimers show that these ions favor extended conformations [59], and collision induced dissociation of  $[Cyt_2+nH]^{n+}$  (where  $n = 18, 20, 22,$  and  $24$ ) leads to highly charged monomers [7], which are known to favor extended conformations [28a,b].

#### *Comparison with Stability of Folded and Unfolded Protein Ion Conformers*

Protein [28, 29] and DNA [54] ions undergo distinct structural transitions from folded to unfolded conformations as the charge state of the ion increases in order to reduce Coulomb repulsion energy. Extensive studies of cytochrome *c* show that the +4 and +5 charge states favor compact conformations. The cross sections for these ions are shown in Figure 9 and fall within the region of stability for a compact conformation. A compact conformation of the +6 ion will fall along the boundary, and a compact form of the +7 and higher charge states should be unstable. Indeed, compact forms of the +4 and +5 charge states are favored under all injection energy conditions and appear to be stable even at buffer gas temperatures of  $\sim 600$  K [60]. Compact states of the +6 and +7 ions can be observed, but only at low injection energies [28(b)]. Studies at high injection voltages (or at high buffer gas temperatures) show that these states are metastable and more open conformations are favored [60]. The stability curve shown in Figure 9 provides an estimate of the transition region from compact to elongated conformations that is in good agreement with these experimental results. The Coulomb transition observed for oligothymidine [54] ( $[T_{10}-nH]^{n-}$ ) is also predicted nicely by Figure 9. Cross sections for  $[T_{10}-2H]^{2-}$  and  $[T_{10}-3H]^{3-}$  ions are  $447 \pm 5$  and  $446 \pm 5 \text{ \AA}^2$ , respectively, and fall within the stable region for the doubly and triply charged lines. The -4, -5, and -6 charge states of DNA favor extended conformations (with cross sections of  $537 \pm 5$ ,  $627 \pm 6$ , and  $641 \pm 6$ , respectively), consistent with the predicted instability of these ions in Figure 9. From this

discussion, it appears that the energy associated with stabilizing high order intermolecular interactions in multimers is similar in magnitude required to stabilize intramolecular interactions in biopolymers. However, in the absence of covalent or strong ionic interactions, these small aggregates dissociate when they are destabilized.

## Summary and Conclusions

Ion mobility techniques have been used to examine the conformations of peptide ions formed by ESI. Under the present experimental conditions (that are typical of many ESI source configurations), peaks in the mass spectra that nominally correspond to singly charged monomer ions were found to be primarily comprised of multiply charged multimers, having a single charge for each monomer unit. Comparison of experimental cross sections with calculated values for trial multimer conformations show that the multimers have tightly packed conformations that are roughly spherical. We have bracketed the density of these ions as  $0.87 < \rho < 1.00 \text{ g cm}^{-3}$ , values that are slightly lower than typical densities for biomolecules in solution [55]. High-resolution ion mobility studies show that there are favored high-order conformations in the gas phase. These conformations appear to be stable over long time scales ( $\sim 0.03$  s). Multimer dissociation can be induced by collisional or thermal excitation. In all of the systems we have studied it appears that the multimers dissociate via loss of singly charged monomer units.

A model based on considerations of Coulomb repulsion energy between multiple charges on the surfaces of spheres has been developed in order to predict the stability of multiply charged multimers. This model predicts that aggregates containing four charges become unstable for species with cross sections below  $\sim 500 \text{ \AA}^2$ . Aggregates containing five and six charges appear to become unstable for species with cross sections smaller than  $\sim 650$  and  $\sim 1150 \text{ \AA}^2$ , respectively.

It is important to note that although multiply charged multimers dominated the ion mobility distributions for the nominal singly charged monomer ions, the mass spectra recorded for these systems showed little or no evidence for multimer formation. Our present results show that multimer formation is favorable for a wide array of different peptides (at least under our ESI source conditions). Thus, for fragmentation and reactivity studies of singly charged monomer ions by mass spectrometric methods, careful measurements of isotopic distributions should be made to ensure the purity of the singly charged monomer ion. Under conditions where multimers are observed, isotopes for the  $m/z = 1061$  ion of bradykinin could not be resolved. Heated capillary inlets and energetic collisions in interfacial pressure regions should also favor the singly charged monomer, and should provide an efficient means of dissociating the multiply charged multimers.

## Acknowledgments

This work was supported by grants from the NSF (grant no. CHE-9625199), NIH (grant no. 1R01GM55647-01), and an ASMS Research Award generously provided by Finnigan MAT. We are grateful to Professor Andrew Ellington for generously donating the LG6 and LG7 peptides.

## References

- Meng, C. K.; Fenn, J. B. *Org. Mass Spectrom.* **1991**, *26*, 542–549.
- Ganem, B.; Li, Y.-T.; Henion, J. D. *J. Am. Chem. Soc.* **1991**, *113*, 6294–6296.
- Ganem, B.; Li, Y.-T.; Henion, J. D. *J. Am. Chem. Soc.* **1991**, *113*, 7818–7819.
- Katta, V.; Chait, B. T. *J. Am. Chem. Soc.* **1991**, *113*, 8534–8535.
- Baca, M.; Kent, S. B. H. *J. Am. Chem. Soc.* **1992**, *114*, 3992–3993.
- Ganguly, A. K.; Pramanik, B. N.; Tsarbopoulos, A.; Covey, T. R.; Huang, E.; Fuhrman, S. A. *J. Am. Chem. Soc.* **1992**, *114*.
- Smith, R. D.; Light-Wahl, K. J.; Winger, B. E.; Loo, J. A. *Org. Mass Spectrom.* **1992**, *27*, 811–821.
- Huang, E. C.; Pramanik, B. N.; Tsarbopoulos, A.; Reichert, P.; Guanguly, A. K.; Trotta, P. P.; Nagabhushan, T. L.; Covey, T. R. *J. Am. Soc. Mass Spectrom.* **1993**, *4*, 624–630.
- Li, Y.-T.; Hsieh, Y.-L.; Henion, J. D.; Ganem, B. *J. Am. Soc. Mass Spectrom.* **1993**, *4*, 631–637.
- Light-Wahl, K. J.; Winger, B. E.; Smith, R. D. *J. Am. Chem. Soc.* **1993**, *115*, 5869–5870.
- Smith, R. D.; Light-Wahl, K. J. *Biol. Mass Spectrom.* **1993**, *22*, 493–501.
- Tang, X.; Brewer, C. R.; Saha, S.; Chernushevich, I.; Ens, W.; Standing, K. G. *Rapid Commun. Mass Spectrom.* **1994**, *8*, 750–754.
- Light-Wahl, K. J.; Schwartz, B. W.; Smith, R. D. *J. Am. Chem. Soc.* **1994**, *116*, 5271–5278.
- Busman, M.; Knapp, D. R.; Schey, K. L. *Rapid Commun. Mass Spectrom.* **1994**, *8*, 211–216.
- Schwartz, B. L.; Bruce, J. E.; Anderson, G. A.; Hofstadler, S. A.; Rockwood, A. S.; Smith, R. D. Chilkoti, A.; Stayton, P. S. *J. Am. Soc. Mass Spectrom.* **1995**, *6*, 459–465.
- Schwartz, B. W.; Gale, D. C.; Smith, R. D. Chilkoti, A.; Stayton, P. S. *J. Mass Spectrom.* **1995**, *30*, 1095–1102.
- Loo, J. A. *J. Mass Spectrom.* **1995**, *30*, 180–183.
- Green, M. K.; Penn, S. G.; Lebrilla, C. B. *J. Am. Soc. Mass Spectrom.* **1995**, *6*, 1247–1251.
- Robinson, C. V.; Chung, E. W.; Knudsen, J.; Aplin, R. T.; Poulsen, F. M.; Dobson, C. M. *J. Am. Chem. Soc.* **1996**, *118*, 8646–8653; Thomson, B. A. *J. Am. Soc. Mass Spectrom.* **1997**, *8*, 1053–1058.
- Stefansson, M.; Sjoberg, P. J. R.; Markides, K. E. *Anal. Chem.* **1996**, *68*, 1792–1797.
- Penn, S. G.; He, F.; Green, M. K.; Lebrilla, C. B. *J. Am. Soc. Mass Spectrom.* **1997**, *8*, 244–252.
- Fenn, J. B.; Mann, M.; Meng, C. K.; Wong, S. F.; Whitehouse, C. M. *Science* **1989**, *246*, 64–71.
- For recent reviews, see (a) Przybylski, M.; Glocker, M. O. *Angew. Chem. Int. Ed. Engl.* **1996**, *35*, 806–826; (b) Smith, R. D.; Bruce, J. E.; Wu, Q.; Lei, Q. P. *Chem. Soc. Rev.* **1997**, *26*, 191–202; (c) Loo, J. A. *Mass Spectrom. Rev.* **1997**, *16*, 1–23.
- Ion mobility spectrometry methods are discussed in the following references: (a) Hagen, D. F. *Anal. Chem.* **1979**, *51*, 870–874; (b) Tou, J. C.; Boggs, G. U. *Anal. Chem.* **1976**, *48*, 1351–1357; (c) Karpas, Z.; Cohen, M. J.; Stimac, R. M.; Wernlund, R. F. *Int. J. Mass Spectrom. Ion Processes* **1986**, *74*, 153–159; (d) St. Louis, R. H.; Hill, H. H. *Cr. Rev. Anal. Chem.* **1990**, *21*, 321–355; (e) von Helden, G.; Hsu, M. T.; Kemper, P. R.; Bowers, M. T. *J. Chem. Phys.* **1991**, *95*, 3835–3837; (f) Jarrold, M. F. *J. Phys. Chem.* **1995**, *99*, 11–21.
- von Helden, G.; Wyttenbach, T.; Bowers, M. T. *Science* **1995**, *267*, 1483–1485; Wyttenbach, T.; von Helden, G.; Bowers, M. T. *J. Am. Chem. Soc.* **1996**, *118*, 8355–8364.
- For recent reviews of ion mobility studies of biomolecules, see: Clemmer, D. E.; Jarrold, M. F. *J. Mass Spectrom.* **1997**, *32*, 577–592; Liu, Y.; Valentine, S. J.; Counterman, A. E.; Hoaglund, C. S.; Clemmer, D. E. *Anal. Chem.* **1997**, *69*, 728A–735A.
- Dugourd, Ph.; Hudgins, R. R.; Clemmer, D. E.; Jarrold, M. F. *Rev. Sci. Instrum.* **1997**, *68*, 1122–1129.
- (a) Clemmer, D. E.; Hudgins, R. R.; Jarrold, M. F. *J. Am. Chem. Soc.* **1995**, *117*, 10141–10142; (b) Shelimov, K. B.; Clemmer, D. E.; Hudgins, R. R.; Jarrold, M. F. *J. Am. Chem. Soc.* **1997**, *119*, 2240–2248; (c) Shelimov, K. B.; Jarrold, M. F. *J. Am. Chem. Soc.* **1997**, *119*, 9586–9587.
- (a) Valentine, S. J.; Clemmer, D. E. *J. Am. Chem. Soc.* **1997**, *119*, 3558–3566; (b) Valentine, S. J.; Anderson, J.; Ellington, A. E.; Clemmer, D. E. *J. Phys. Chem. B* **1997**, *101*, 3891–3900; (c) Valentine, S. J.; Counterman, A. E.; Clemmer, D. E. *J. Am. Soc. Mass Spectrom.* **1997**, *8*, 954–961.
- Qin, J.; Chait, B. T. *J. Am. Chem. Soc.* **1995**, *117*, 5411–5412; Shevchenko, A.; Wilm, M.; Vorm, O.; Mann, M.; *Anal. Chem.* **1996**, *68*, 850–858; Wilm, M.; Shevchenko, A.; Houthaevae, T.; Breit, S.; Schweigerer, L.; Fotsis, T.; Mann, M. *Nature* **1996**, *379*, 466–469; Shevchenko, A.; Jensen, O. N.; Podtelejnikov, A. V.; Sagliocco, F.; Wilm, M.; Vorm, O.; Mortensen, P.; Boucherie, H.; Mann, M. *Proc. Natl. Acad. Sci. USA* **1996**, *93*, 14440–14445; Figeys, D.; Ducret, A.; Yates, Y. R., III; Aebersold, R. *Nat. Biotechnol.* **1996**, *14*, 1579–1583; Neubauer, G.; Gottschalk, A.; Fabrizio, P.; Seraphin, B.; Luhrmann, R.; Mann, M. *Proc. Natl. Acad. Sci. USA* **1997**, *94*, 385–390; Qin, J.; Fenyö, D.; Zhao, Y.; Hall, W. W.; Chao, D. M.; Wilson, C. J.; Young, R. A.; Chait, B. T. *Anal. Chem.* **1997**, *69*, 3995–4001.
- Loo, J. A.; Edmonds, C. G.; Udseth, H. R.; Smith, R. D. *Anal. Chim. Acta* **1990**, *241*, 167–173; Rockwood, A. L.; Busman, M.; Udseth, H. R.; Smith, R. D. *Rapid Commun. Mass Spectrom.* **1991**, *5*, 582–585; Busman, M.; Rockwood, A. L.; Smith, R. D. *J. Phys. Chem.* **1992**, *96*, 2397–2400; Senko, M. W.; Speir, J. P.; McLafferty, F. W. *Anal. Chem.* **1994**, *66*, 2801–2808; Little, D. P.; Speir, J. P.; Senko, M. W.; O'Connor, P. B.; McLafferty, F. W. *Anal. Chem.* **1994**, *66*, 2809–2815; Marzluff, E. M.; Campbell, S.; Rodgers, M. T.; Beauchamp, J. L. *J. Am. Chem. Soc.* **1994**, *116*, 7787–7796; Meot-Ner (Mautner), M.; Dongré, A. R.; Somogyi, Á.; Wysocki, V. H. *Rapid Commun. Mass Spectrom.* **1995**, *9*, 829–836; Price, W. D.; Schnier, P. D.; Williams, E. R. *Anal. Chem.* **1996**, *68*, 859–866; Price, W. D.; Schnier, P. D.; Jockusch, R. A.; Williams, E. R. *J. Am. Chem. Soc.* **1996**, *118*, 10640–10644.
- Covey, T. R.; Douglas, D. J. *J. Am. Soc. Mass Spectrom.* **1993**, *4*, 616–623; Cox, K. A.; Julian, R. K.; Cooks, R. G.; Kaiser, R. E. *J. Am. Soc. Mass Spectrom.* **1994**, *5*, 127–136; Chen, Y.-L.; Collings, B. A.; Douglas, D. J. *J. Am. Soc. Mass Spectrom.* **1997**, *8*, 681–687; Collings, B. A.; Douglas, D. J. *J. Am. Chem. Soc.* **1996**, *118*, 4488–4489.
- Kaltashov, I. A.; Fenselau, C. C. *J. Am. Chem. Soc.* **1995**, *117*, 9906–9910; Adams, J.; Strobel, F.; Reiter, A. *J. Am. Soc. Mass Spectrom.* **1996**, *7*, 30–41; Kaltashov, I. A.; Fenselau, C. C. *Proteins* **1997**, *27*, 165–170.
- Sullivan, P. A.; Axelsson, J.; Altmann, S.; Quist, A. P.; Sunqvist, B. U. R.; Reimann, C. T. *J. Am. Soc. Mass Spectrom.* **1996**, *7*, 329–341.
- Winter, B. E.; Light-Wahl, K. J.; Rockwood, A. L.; Smith, R. D. *J. Am. Chem. Soc.* **1992**, *114*, 5897–5898; Suckau, D.; Shi, Y.; Beu, S. C.; Senko, M. W.; Quinn, J. P.; Wampler, F. M.; McLafferty, F. W. *Proc. Natl. Acad. Sci. USA* **1993**, *90*, 790–793; Wood, T. D.; Chorush, R. A.; Wampler, F. M.; Little, D. P.; O'Connor, P. B.; McLafferty, F. W. *Proc. Natl. Acad. Sci. USA* **1995**, *92*, 2451–

- 2454; Cassady, C. J.; Carr, S. R. *J. Mass Spectrom.* **1996**, *31*, 247-254.
36. Schnier, P. F.; Gross, D. S.; Williams, E. R. *J. Am. Chem. Soc.* **1995**, *117*, 6747-6757; Williams, E. R. *J. Mass Spectrom.* **1996**, *31*, 831-842.
37. Rodriguez-Cruz, S. E.; Klassen, J. S.; Williams, E. R. *J. Am. Soc. Mass Spectrom.* **1997**, *8*, 565-568.
38. Fye, J. L.; Woenckhaus, J.; Jarrold, M. F. *J. Am. Chem. Soc.*, 1998, *120*, 1327-1328.
39. Jarrold, M. F.; Honea, E. C.; *J. Phys. Chem.* **1991**, *95*, 9181-9185; Jarrold, M. F.; Constant, V. A. *Phys. Rev. Lett.* **1991**, *67*, 2994-2997.
40. Liu, Y.; Clemmer, D. E. *Anal. Chem.* **1997**, *69*, 2504-2509.
41. Wittmer, D.; Chen, Y. H.; Luckenbill, B. K.; Hill, H. H., Jr. *Anal. Chem.* **1994**, *66*, 2348-2355; Chen, Y. H.; Hill, H. H., Jr.; Wittmer, D. P. *Int. J. Mass Spectrom. Ion Processes* **1996**, *154*, 1-13; Hudgins, R. R.; Woenckhaus, J.; Jarrold, M. F. *Int. J. Mass Spectrom. Ion Processes* **1997**, *165/166*, 497-507; Guevremont, R.; Siu, K. W. M.; Wang, J.; Ding, L. *Anal. Chem.* **1997**, *69*, 3959-3965.
42. Equipotential lines were calculated using: SIMION 3D, Idaho National Engineering Laboratory, Idaho Falls, ID, 1994.
43. Hoaglund, C. S.; Valentine, S. J.; Sporleder, C. R.; Reilly, J. P.; Clemmer, D. E., *Anal. Chem.*, in press.
44. Insulin chain A has the sequence GIVEQZZASVZSLYQLE-NYZN, where Z corresponds to an oxidized cysteine residue.
45. Mason, E. A.; McDaniel, E. W. *Transport Properties of Ions in Gases*. Wiley: New York, 1988.
46. Mesleh, M. F.; Hunter, J. M.; Shvartsburg, A. A.; Schatz, G. C.; Jarrold, M. F. *J. Phys. Chem.* **1996**, *100*, 16082-16086; Wyttenbach, T.; von Helden, G.; Batka, J. J., Jr.; Carlat, D.; Bowers, M. T. *J. Am. Soc. Mass Spectrom.* **1997**, *8*, 275-282.
47. Shvartsburg, A. A.; Jarrold, M. F. *Chem. Phys. Lett.* **1996**, *261*, 86-91.
48. Revercomb, H. E.; Mason, E. A. *Anal. Chem.* **1975**, *47*, 970.
49. Under low field conditions, the diffusion constant is related to the measured mobility by the expression  $D = Kk_bT/ze$ , where  $K$  is the mobility,  $k_b$  is Boltzmann's constant, and  $ze$  is the charge.
50. The peak at  $m/z = 500$  for BK was not observed in other mass spectra recorded under identical conditions and is probably a noise spike.
51. Recent studies of the bradykinin system in our ion mobility/TOF instrument show that at high injection voltages doubly charged  $[M+2H]^{2+}$  ions may convert into singly charged  $[M+H]^+$  ions. This presumably occurs at high injection voltages via an endothermic process that forms  $HeH^+$ .
52. As shown in eq 3, the theoretical resolving power increases as the square root of the ion charge state.
53. Schnier, P. D.; Price, W. D.; Jockusch, R. A.; Williams, E. R. *J. Am. Chem. Soc.* **1996**, *118*, 7178-7189.
54. Hoaglund, C. S.; Liu, Y.; Pagel, M.; Ellington, A. D.; Clemmer, D. E. *J. Am. Chem. Soc.* **1997**, *119*, 9051-9052.
55. *Handbook of Biochemistry and Molecular Biology*, 3rd ed; Fasman, G. D., Ed.; Cleveland, OH: Chem. Rubber, 1975; pp 429; *Methods in Enzymology*, vol. 259; Johnson, M. L.; Ackers, G. K., Eds.; New York: Academic, 1995; pp 385.
56. Counterman, A. E.; Samuelson, S.; Martyna, G. J.; Clemmer, D. E., unpublished.
57. The mechanism associated with ion formation during the final stages of ESI is an area of active debate. Two models that have been discussed are the charged residue model (Dole, M.; Mack, L. L.; Hines, R. L.; Mobley, R. C.; Fergusson, L. P.; Alice, M. B. *J. Chem. Phys.* **1968**, *49*, 2240-2249) and the ion evaporation model (Iribarne, V.; Thompson, B. A. *J. Chem. Phys.* **1976**, *64*, 2287-2294).
58. The coulomb repulsion energies for  $n$  charges is calculated from

$$C.E. = \sum_{i=1}^{n-1} \sum_{j=i+1}^n \frac{q^2}{4\pi\epsilon_0\epsilon r_{ij}}$$

where  $\epsilon_0$  is the permittivity of free space, and  $\epsilon$  is the dielectric constant, and  $r_{ij}$  is the distance between charges assigned to the  $i$  and  $j$  locations. Charges were assigned to locations that minimize the Coulomb energy for a sphere containing from 2 to 8 charges. The dielectric constant is unknown; therefore, we have used a value of 2.0, as reported for gas-phase cytochrome  $c$  in [36].

59. Valentine, S. J.; Clemmer, D. E., unpublished results.
60. Woenckhaus, J.; Hudgins, R. R.; Jarrold, M. F., unpublished.